Supplemental material for : "Soliton refraction by an optical soliton gas"

Pierre Suret,[1] Martin Dufour,[1] Giacomo Roberti,[2] Gennady El,[2] François Copie,[1] and Stéphane Randoux[1,*]

[1] *Univ. Lille, CNRS, UMR 8523 - PhLAM - Physique des Lasers Atomes et Molécules, F-59 000 Lille, France*
[2] *Department of Mathematics, Physics and Electrical Engineering, Northumbria University, Newcastle upon Tyne, NE1 8ST, United Kingdom*

(Dated: July 18, 2023)

The purpose of this Supplemental Material is to provide some details about the experimental setup and about the experimental methodology. We also briefly discuss annex questions about the influence of the strength of the initial noise and about the analogy between soliton refraction and refraction of light rays. All equations, figures, reference numbers within this document are prepended with "S" to distinguish them from corresponding numbers in the Letter.

CONTENTS

I. DETAILED DESCRIPTION OF THE EXPERIMENTAL SETUP

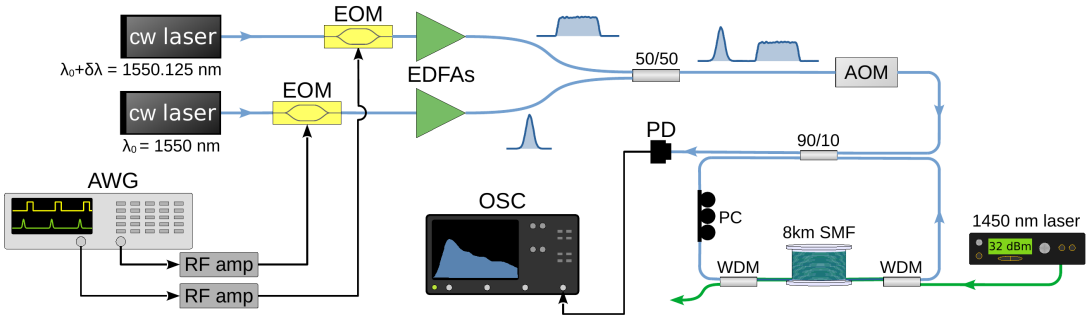

FIG. S1. Schematic representation of the experimental setup. The light signals are shaped using two intensity modulators (EOM) driven independently by the two synchronized channels of an arbitrary waveform generator (AWG) having a bandwidth of 25 GHz. The optical signals are amplified to Watt-level using Erbium-doped fiber amplifiers (EDFAs) before being combined via a 50/50 fiber coupler and injected inside the recirculating fiber loop. Light detection is made using a fast photodiode (PD) coupled to a fast oscilloscope (OSC) having a bandwidth of 65 GHz and a sampling frequency of 160 GSa/s.

* stephane.randoux@univ-lille.fr

Fig. S1 shows a detailed representation of our experimental setup, including some technical details about the generation of the optical signals that are not described in the Letter. The light source used for generation of the short light pulses is a single-frequency continuous-wave (CW) laser diode (APEX-AP3350A) centered at $\lambda_0 = 1550$ nm which delivers an optical power of a few mW. The short pulses are produced by using a 20-GHz intensity modulator (iXblue MX-LN-20) connected to an arbitrary waveform generator (AWG) having a bandwidth of 25 GHz.

The optical soliton gases (SGs) are made using another intensity-modulated laser at the wavelength $\lambda_0 + \delta\lambda$ with $\delta\lambda = 0.125$ nm. The SGs have the initial form of flat-top pulses with durations that increase monotonically from $\sim$ 200 ps to $\sim$ 2000 ps in 29 steps. These flat-top pulses are produced using an intensity modulator connected to the second channel of the AWG. This second channel is synchronized with the first channel of the AWG. The initial delay between the short pulses and the flat-top pulses (the optical SGs) can be adjusted with a resolution of 20 ps by controlling the shapes and delays of the electrical signals delivered by the each of the two channels of the AWG.

In our experiment the short pulse and the optical SG have slightly different group velocities because the wavelength of the laser that this used to generate the optical SG is detuned by $\delta\lambda$ from the wavelength of the laser used to generate to short pulses. The group velocity difference δv_g between the short pulse and the SG is given by $[\delta v_g]^{-1} \simeq (2\pi c/\lambda_0^2)\beta_2\,\delta\lambda \simeq -2.16$ ps/km where c represent the velocity of light in vacuum. The group velocity dispersion coefficient of the fiber is $\beta_2 = -22$ ps^2 km^{-1} at the wavelength $\lambda_0 = 1550$ nm.

The short pulses and flat-top pulses are amplified at the Watt-level by using Erbium-doped fiber amplifiers (EDFAs). Importantly the amplified spontaneous emission (ASE) of the EDFA amplifying the power of the flat-top pulses adds some optical noise, which explains that the generated square pulses evolve into fully randomized SGs inside the recirculating fiber loop.

The light signals at the output of the EDFA are combined using a 50/50 fused fiber coupler connected to an acousto-optic modulator (AOM). The AOM plays the role of an optical gate that is open during $\sim$ 500 ns for the injection of the light signal into the fiber loop and closed over much longer times (typically $\sim$ 5 ms), when the signal circulates inside the fiber loop.

The recirculating fiber loop is made of $\sim$ 8 km of single mode fiber (SMF) closed on itself by a 90/10 fiber coupler. The SMF has been manufactured by Draka-Prysmian. It has a measured second-order dispersion coefficient $\beta_2 = -22$ ps^2 km^{-1} and an estimated Kerr coefficient $\gamma = 1.3$ km^{-1} W^{-1} at the working wavelength of 1550 nm.

The 90/10 coupler is arranged in such a way that 90% of the intracavity power is recirculated. The optical signal circulates in the counter-clockwise direction. At each round trip, 10% of the circulating power is extracted and directed toward a photodetector (PD) coupled to a sampling oscilloscope (160 Gsa/s) leading to an overall 32 GHz detection bandwidth. Experimental data consist in a succession of sequences (one per round trip) that are subsequently processed numerically to construct single-shot space-time diagrams showing the wavefield dynamics.

The losses accumulated over one circulation in the fiber loop are partially compensated using a counter-propagating Raman pump at 1450 nm coupled in and out of the loop via wavelength division multiplexers (WDMs). The pump laser at 1450 nm is a commercial Raman fiber laser delivering an output beam having a power of several Watt. In our experiments, this optical power is attenuated to typically $\approx$ 200 mW by using a 90/10 fiber coupler (not shown in Fig. S1). The mean optical power decay rate of the field circulating in the loop is $\alpha_{eff} \sim 6.2 \times 10^{-4}$ km^{-1} or equivalently ~ 0.0027 dB/km.

II. CIRCULATING OPTICAL SIGNAL AND OPTICAL POWER CALIBRATION

In this Section, we show and describe the characteristics of the entire optical signal that circulates inside the fiber loop.

Fig. S2(a) shows the space-time evolution of the entire signal circulating inside the loop. It has a duration of $\sim$ 400 ns and it propagates over a distance of $\sim$ 1500 km (the propagation time in one experiment is around 5 ms). As described in the Letter, the optical signal is composed of an ensemble of 29 short pulses, each of them being followed by its own SG that has the initial shape of a flat-top pulse perturbated by some optical noise (see Fig. S2(b)–(e)).

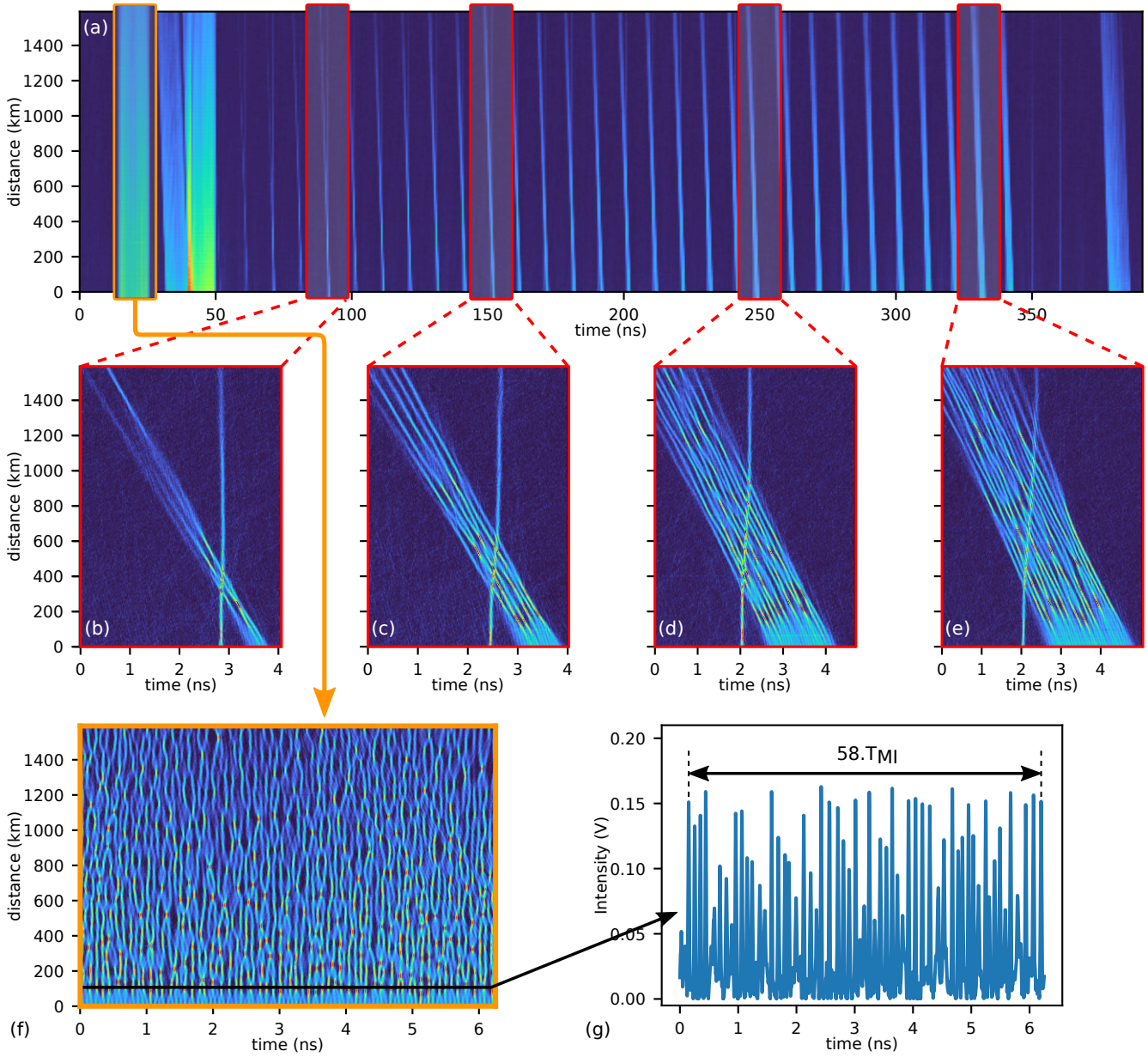

FIG. S2. (a) Global space-time pattern recorded at the output of the recirculating fiber loop in a single shot. The region where 29 solitons interact with 29 optical SGs is between $t \simeq 60$ ns and $t \simeq 340$ ns. (b)–(e) Zoomed view on four selected experiments where solitons are refracted by SGs of various extensions. (f) Space-time evolution of a broad pulse of constant power initially pertubated by some optical noise. This space-time pattern is typical from evolution observed in the so-called nonlinear stage of MI. The optical signal measured at $z = 96$ km and shown in (f) is used to determine the mean power of the broad pulse. This measurement is used to calibrate the optical power circulating in the fiber loop.

In Fig. S2(a), the time interval devoted to experiments where solitons interact with SGs ranges between $t \simeq 60$ ns and $t \simeq 340$ ns. Between these two times, the duration of the SGs increases monotonically from ~ 200 ps to ~ 2000 ps (right part of Fig. S2 around $t = 330$ ns) in 29 steps. Using this strategy, we capture in one single shot the space-time evolution of a set of 29 experiments where we observe the interaction between 29 pulses and 29 associated SGs of increasing extents. This "single-shot approach" has the advantage of avoiding any significant drift in the experimental parameters during the whole experiment (~ 5 ms). All the 29 experiments (and the associated shift measurements) are made in the same conditions with identical physical parameters. Also, we note that the time separation between two neighboring experiments is sufficiently large to guarantee that all the experiments are independent (i. e. long-range coupling between one given experiment and the 28 others are fully negligible).

In addition to the broad space-time region where solitons interact with SGs, the optical signal propagating inside the fiber loop has also been designed to incorporate some other regions that permit to measure the optical power circulating inside the fiber loop with a good accuracy. The region in Fig. S2(a) that is surrounded by an orange rectangle is the region of propagation of a very broad ($\sim$ 10 ns) flat top pulse perturbated by some small optical noise. As clearly shown in Fig. S2(f), the flat-top part of the pulse behaves as a plane wave that is destabilized by the small optical noise through the process of modulation instability (MI), as already shown and extensively discussed in ref. [1].

The observed evolution of the nonlinear stage of MI can be used to advantage to measure the optical power circulating inside the fiber loop. Fig. S2(g) shows the time signal recorded after a propagation distance of $z = 96$ km, at a point where large coherent structures can be observed after the initial destabilization of the plane wave. The number of coherent structures observed on a given time span is directly dependent on the period T_{MI} associated with the process of MI. In Fig. S2(g), we record a total of 58 coherent structures over a time span of 6.05 ns, which means that the period associated with the MI process is T_{MI} =104.3 ps. Therefore the mean power P_0 of the plane wave in the measurement region is given by $P_0 = (2\pi/T_{MI})^2|\beta_2|/(2\gamma) = 29$ mW [1]. This value is used for calibration and permits to convert the voltage measured by the fast photodiode into an optical power.

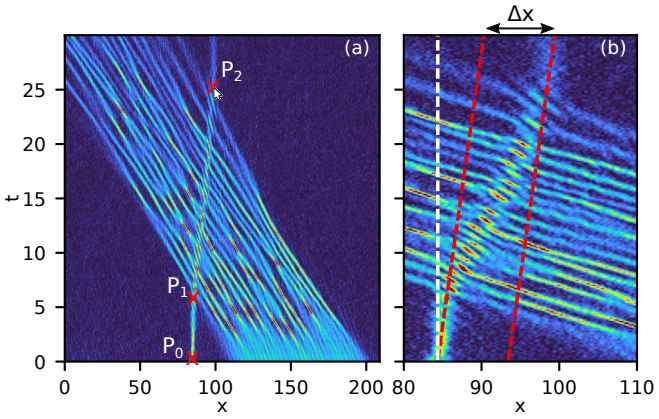

FIG. S3. (a) Experimental space-time diagram showing the positions of the points $P_i(x_i, t_i)$ $(i = 0, 1, 2)$ that are measured in order to determine the space shift (Δx) due to the refraction phenomenon. (b) Zoomed view of (a) showing the measured shift Δx.

III. MEASUREMENT OF THE SPACE SHIFT IN EXPERIMENTS

In this section we describe how the space shift associated with the refraction of the soliton by the SGs has been measured in the experiment.

In a first step, the space-time diagrams recorded in the experiment are converted to dimensionless units using mathematical transformations given in the Letter, see Eq. (3). In a second step, the position (x_i, t_i) of the soliton is measured at three different times $(i = 0, 1, 2)$. The first measurement point is the point $P_0(x_0, t_0)$ in Fig. 3(a) that corresponds to the smallest time at which the soliton position can be measured. The second measurement point is the point $P_1(x_1, t_1)$ in Fig. S3(a) that corresponds to the soliton position just before it is refracted in the SG. The third measurement point is the point $P_2(x_2, t_2)$ in Fig. 3(a) that corresponds to the soliton position just after it emerges from the SG.

The position shift Δx computed from simple trigonometric considerations is given by

$$\Delta x = x_2 - x_0 - t_2 \tan(\alpha) \tag{S1}$$

with $\tan(\alpha) = \frac{x_1 - x_0}{t_1 - t_0}$.

There exists an uncertainty in positioning P_0, P_1, P_2 in the space-time plot shown in Fig. S3. This uncertainty translates into an error on the shift Δx that is measured experimentally. We have estimated it in a statistical way by repeating the measurement of the positions of P_0, P_1, P_2 a large number of times. Doing that (i.e. repeating 50 times

the same measurement of the shift in one given experiment), we estimate that the absolute error on the measurement of the position shift Δx of the tracer soliton is ± 0.5.

Let us emphasize that there also exists some uncertainties on the shift measurement in our numerical simulations. One source of uncertainty arises from the fact that we make some assumptions about the mathematical form of the function fitting the noisy pulses that are recorded in the experiments. In the Letter, we have chosen to fit the experimental pulses by gaussian pulses. If another choice like sech-like pulses is made, we have found that the imaginary part η_p of the spectral parameter characterizing the pulse can change by $\sim 10\%$ (with the area $\mathcal{A}_p$ being constant). However the relative change of spatial shift arising from this modification of the pulse eigenvalue is typically only around $\sim 2\%$. Nevertheless the measurement of the position shift Δx in our numerical simulations of Eq. (3) is made using the same procedure as the one used for experimental data and we estimate that the absolute error made in the measurement of the numerical shifts is similar to the error made in the experimental measurement.

IV. EXPERIMENTAL MEASUREMENT OF THE PULSE AREAS AND NUMERICAL CALCULATION OF THE ASSOCIATED DISCRETE IST SPECTRA

Fig. S4 shows a typical signal that is recorded in the experiment after a propagation over one round-trip ($z = 8$ km). In the example shown in Fig. S4, the signal is plotted in dimensionless units. It consists of one pulse located near one of the SGs of largest extension. The signal plotted with a gray line is the raw signal recorded by the fast photodiode. The fast oscillations at a frequency of ~ 15 GHz that are detected on the top of the square pulse are due to the beating between the laser used to produce the short pulses and the laser used to produce the square pulses (the optical SGs).

The extinction ratio of the EOMs (see Fig. S1) is of 20 dB. This means that residual light carrying a power that is $\sim 1\%$ smaller than the power of the modulated signals propagate with the square and pulsed signals produced by the modulators. This produces a spectacular beating pattern on the top of the square pulses which represents however an observation artifact. In particular, the observed beating signal has no influence on the solitonic content of the pulses.

In order to measure the area of the square pulses, the beating signal is suppressed by using a filter that smooth the unwanted oscillation at ~ 15 GHz. This gives the signal plotted with the black line in Fig. S4. The area $\mathcal{A}_{SG}$ under the black line defined by $\mathcal{A}_{SG} = \int |\psi(x)| dx$ is then easily computed. As described in the Letter, this signal in black line is then fitted by the function $\psi_{SG}(x) = b \exp\left(-x^{2n}/(2L^{2n})\right)$ where the real parameters b, x_0, L and the integer parameter n are determined under the constraint that the integral $\int |\psi_{SG}(x)| dx$ must be equal to the area $\mathcal{A}_{SG}$ that has been measured for the experimental signal.

The same procedure is used for the short pulse except that the filtering stage is not applied. The measured profile is fitted by $\psi_p(x) = a \exp\left(-x^2/(2w^2)\right)$, where the parameters a and w are determined under the constraint that the integral $\int |\psi_P(x)| dx$ must be equal to the area $\mathcal{A}_P = \int |\psi(x)| dx$ measured for the short pulse in the experiment.

Once the parameters characterizing the experimental pulses ((a, w) and (b, L, n)) are determined, their discrete IST spectra are computed numerically using the Fourier collocation method described in ref. [2].

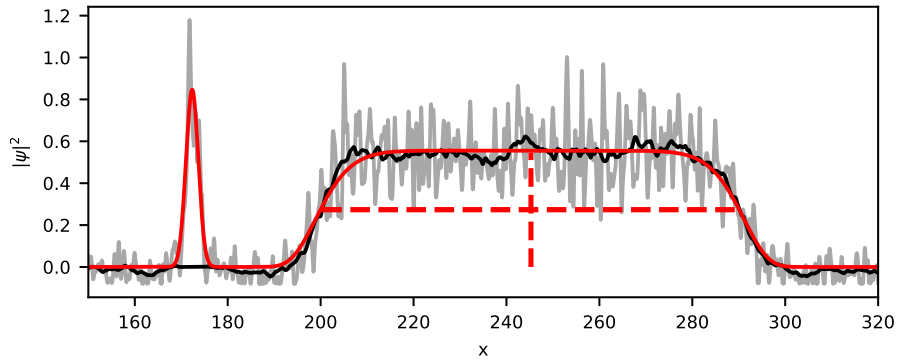

FIG. S4. Raw signal recorded in the experiment (gray line) plotted in dimensionless units. The black line represents the raw signal that has been smoothed to remove unwanted oscillations due to the beating between the two laser fields. The red line represents the functions $\psi_p(x)$ and $\psi_{SG}(x)$ that are fitted from the experimental data.

V. NUMERICAL VALUES OF THE FITTING PARAMETERS AND OF THE SPACE SHIFTS CHARACTERIZING EACH OF THE 29 EXPERIMENTS

In this section we provide a table summarizing the parameters fitting the tracer pulses and the square pulses together with the space shift measured in the experiments and in the numerical simulations of the 1D-NLSE (Eq. (3) of the manuscript).

	a	w	η_p	b	L	n	$\Delta x(EXP)$	$\Delta x(NLSE)$
1	1.08	1.57	0.734	0.427	4.83	2	0.13	0.75
2	1.10	1.21	0.643	0.535	5.45	2	0.57	1.16
3	1.07	1.45	0.693	0.585	6.78	2	0.89	1.61
4	0.92	1.92	0.636	0.533	8.22	2	1.20	1.73
5	0.94	1.83	0.646	0.603	9.74	4	2.06	2.19
6	1.00	1.77	0.698	0.597	10.72	4	2.73	2.50
7	1.02	1.74	0.714	0.600	13.02	4	2.56	3.03
8	0.97	1.87	0.682	0.678	15.07	6	3.36	4.08
9	0.99	1.78	0.687	0.658	16.11	6	3.94	4.12
10	1.03	1.59	0.685	0.600	17.91	6	2.91	4.26
11	1.06	1.49	0.696	0.614	19.51	6	3.70	4.72
12	0.96	1.67	0.635	0.595	21.59	6	4.06	5.31
13	1.05	1.80	0.751	0.568	22.47	6	5.20	5.00
14	1.23	1.31	0.814	0.558	24.22	8	4.17	5.40
15	1.12	1.45	0.740	0.544	25.75	10	5.34	5.81
16	1.00	1.82	0.710	0.542	26.46	10	5.20	5.78
17	1.05	1.74	0.741	0.560	28.57	10	5.83	6.51
18	1.09	1.42	0.704	0.551	29.97	12	5.20	6.86
19	1.08	1.72	0.772	0.573	31.36	12	6.24	7.68
20	1.06	1.50	0.698	0.603	33.64	12	6.75	8.50
21	1.04	1.66	0.712	0.571	36.47	10	7.66	8.67
22	1.16	1.53	0.807	0.566	37.41	10	8.76	8.55
23	1.08	1.67	0.756	0.559	39.23	12	8.23	9.08
24	1.01	1.82	0.720	0.584	40.50	14	9.68	10.01
25	1.07	1.75	0.762	0.584	41.92	14	9.25	10.30
26	1.07	1.76	0.764	0.587	42.00	10	8.81	9.95
27	1.13	1.46	0.758	0.598	43.51	10	9.42	10.65
28	0.95	1.65	0.617	0.603	44.75	10	10.10	11.70
29	0.97	2.04	0.710	0.634	46.78	10	11.37	12.64

TABLE I. For each of the 29 experiments presented in Fig. S2(a), this table summarizes the parameters fitting the amplitude a and the width w of the tracer pulses that are described by the discrete eigenvalue $\lambda_p = -v/4 + i\eta_p$ ($v = 4.74$). It also summarizes the amplitude b and the width L of the square pulses together with the exponent n used to fit the pulses by a super-gaussian function, see Sec. IV. The numerical values of the shift Δx measured in the experiment and in the numerical simulation of Eq. (3) are given in the two last columns on the right.

VI. INFLUENCE OF THE STRENGTH OF THE INITIAL NOISE PERTURBING THE SQUARE PULSE ON THE SPACE SHIFT EXPERIENCED BY THE TRACER SOLITON

In our experiment, the optical SG has initially the form of a "long" square pulse perturbed by some optical noise that is added by the EDFA, see Sec. I. In this Section, we show that the strength of this initial noise does not significantly influence the position shift experienced by the tracer soliton.

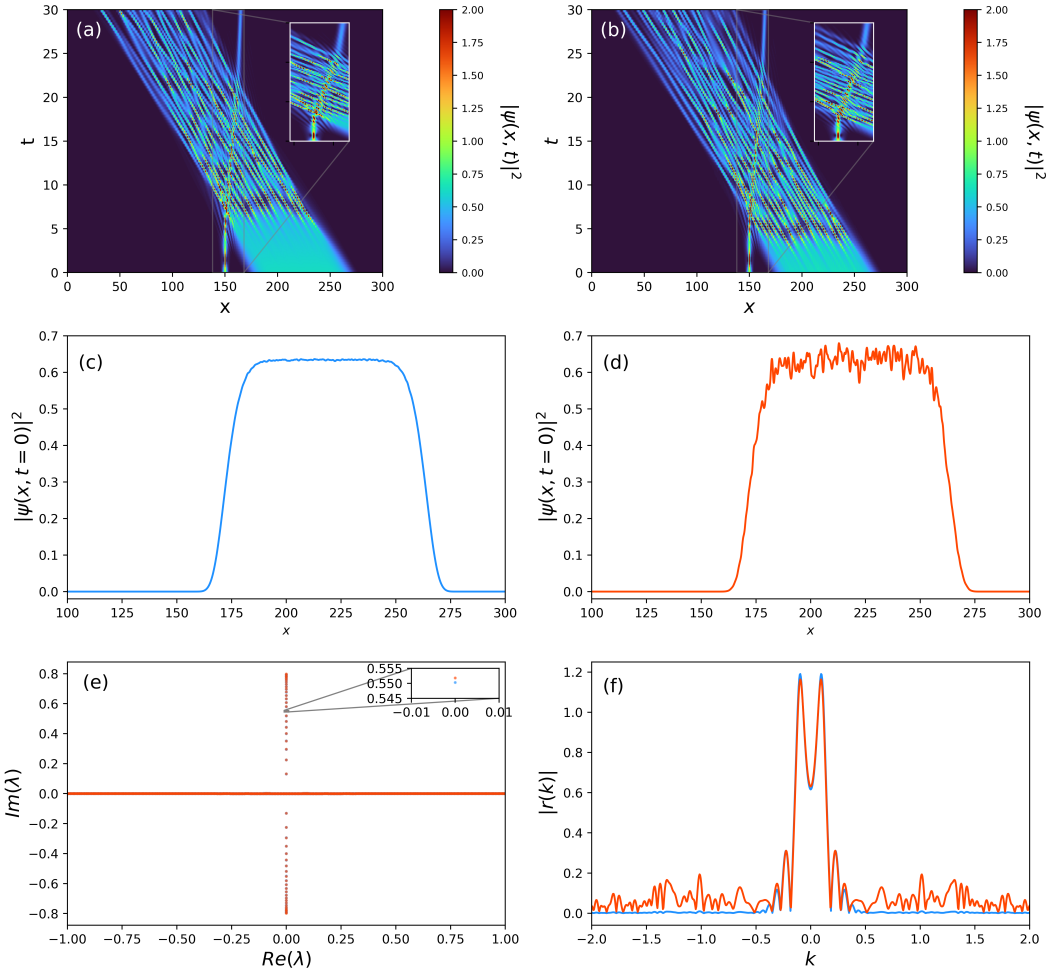

FIG. S5. (a) Numerical simulation of Eq. (3) of the manuscript with the initial condition being the square pulse perturbed by a small noise represented in (c). (b) Same as in (a) but with the square pulse represented in (d) and perturbed by a strong noise. (e) Discrete IST spectral of the square pulse shown in (c) (blue points) and in (d) red points). (f) Continuous spectrum of the square pulse shown in (c) (blue line) and in (d) (red line).

Fig. S5 shows numerical simulations of the 1D-NLSE (Eq. (3) of the manuscript with $\epsilon = 0.016$) where square pulses are perturbed initially by noise having two different levels, compare Fig. S5(c) and Fig. S5(d). As shown in Fig. S5(a) and Fig. S5(b), the spatio-temporal evolutions that are observed with these two different initial conditions are very similar. It is noticeable that the development of a fully randomized bound state SG occurs at a short time ($t \sim 1$) when the square pulse is initially perturbed by a strong noise, see Fig. S5(b). On the other hand, it occurs at a longer time ($t \sim 5$) when the initial noise is small, see Fig. S5(a). However the space shift Δx that is observed due to the interaction between the tracer soliton and the SG is nearly identical in the two NLSE simulations (compare the insets in Fig. S5(a) and Fig. S5(b)).

The fact that the space shift Δx does not significantly depend on the noise level can be understood from simple considerations from the IST theory. Fig. S5(e) shows the discrete IST spectra the square pulse perturbed by a small noise (blue points) and by a strong noise (red points). It can be readily seen that the discrete IST spectra are nearly identical for both pulses, whatever their noise level. On the other hand, the continuous spectra (or reflection coefficients in the IST theory) of the two square pulses significantly differ: the continuous spectrum of the noisiest

pulse is significantly perturbed by the presence of the strong random fluctuations on the top of the pulse.

Summarizing, the noise perturbing the square pulses dominantly influences the continuous part of the IST spectrum associated with dispersive waves without perturbing significantly the discrete part of the IST spectrum that is associated with solitonic modes.

The numerical simulation shown in Fig. S5 confirms that the observed space shift dominantly arises from the interaction between solitonic modes, as described by Eq. (5) of the manuscript. This information is also present in Fig. 3(a) of the manuscript where most of the points computed from Eq. (5) are very close to those computed from the numerical simulation of the 1D-NLSE.

VII. ANALOGIES AND DIFFERENCES BETWEEN SOLITON REFRACTION AND REFRACTION OF LIGHT RAYS

In this section, we briefly discuss the analogies and differences that can be drawn between the soliton refraction phenomenon evidenced in our work and the conventional refraction of light rays in geometrical optics.

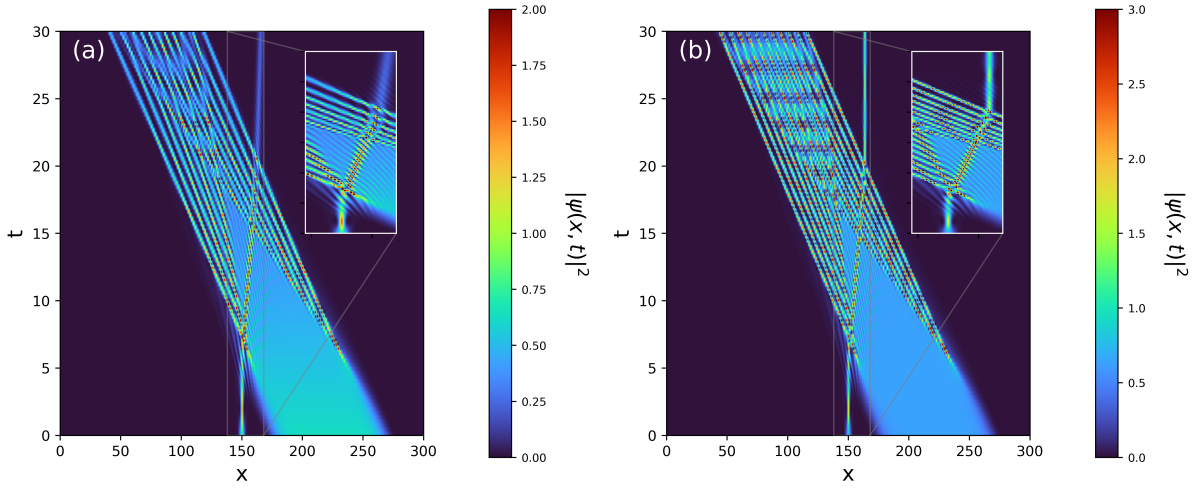

FIG. S6. (a) Space-time plot computed from numerical simulations of 1D-NLSE with a small damping term (Eq. (3) of the manuscript with $\epsilon = 0.016$). (b) Same as in (a) but without dissipation ($\epsilon = 0$ in Eq. (3)).

In geometrical optics, the refraction of light rays occurs at the interface between two dielectric media having refractive indexes n_1 and n_2. This phenomenon is described by the so-called Snell-Descartes law that connects the angle of refraction α_2 of the light ray with its angle of incidence α_1 ($\sin(\alpha_2) = n_1/n_2 \sin(\alpha_1)$). The Snell-Descartes law describes some linear physics where the refraction phenomenon does not depends on the intensity of the light beams.

In our work with solitons, we observe an intrinsically nonlinear phenomenon where the "angle of refraction" depends not only on the "angle of incidence" but also on the optical powers carried by the tracer soliton and the SG. Taking the perspective of geometrical optics, the refraction angle would be the effective velocity $s(\eta_p)$ of the tracer soliton propagating inside the SG while the incidence angle would be the relative velocity v between the free (non-interacting) tracer soliton and the SG. The relation analogous to Snell-Descartes law would be Eq. (7) of the manuscript that simplifies into Eq. (8) for the bound state SG realized in our experiment (still keeping the analogy with ray optics, this bound state SG represents a glass slide).

Eq. (8) of the manuscript indicates how the effective velocity (or refraction angle) of the tracer soliton (or light ray) is modified due to the interaction with the SG (or glass slide). $s(\eta_p)$ is a function of v (the "incidence angle"), of η_p (the parameter encoding the amplitude and width of the tracer soliton) and of b (the parameter giving the amplitude of the initial noisy square pulse that develops into a SG).

Considering the refraction of a light ray through a glass slide in geometrical optics, it is well known that the incident ray and the emergent ray are parallel to each other. The transmission through the glass slide results in a position shift of the light ray for non-zero incidence angles. As illustrated in Fig. S6 showing numerical simulations of the 1D-NLSE (Eq. (3) of the manuscript), the tracer soliton emerges from the SG with a direction that is parallel to the incident one only if the evolution is governed by the integrable (non-dissipative) 1D-NLSE, see Fig. S6(b). On the

other hand, collisions or interactions between solitons becomes inelastic in the presence of a small dissipation, which results in "refraction" and "incidence" angles that are different, as illustrated in Fig. S6(a). Note also that Eq. (8) of the manuscript indicates that the position shift of the tracer soliton grows with the number of solitons in the SG (and with its spatial extension).

[S1] A. E. Kraych, D. Agafontsev, S. Randoux, and P. Suret, Statistical properties of the nonlinear stage of modulation instability in fiber optics, Phys. Rev. Lett. **123**, 093902 (2019).

[S2] J. Yang, *Nonlinear Waves in Integrable and Non-integrable Systems*, Mathematical Modeling and Computation (Society for Industrial and Applied Mathematics, 2010).